Geochemistry Geophysics Geosystems G3

Article
Volume 11, Number 8
14 August 2010
Q08S26, doi:10.1029/2009GC002936
ISSN: 1525-2027

Published by AGU and the Geochemical Society

Imaging crustal structure in south central Costa Rica with receiver functions

Y. Dzierma, M. M. Thorwart, and W. Rabbel
Abteilung Geophysik, Institut für Geowissenschaften, SFB 574, Christian-Albrechts-Universität zu Kiel, Otto-Hahn-Platz 1, D-24118 Kiel, Germany (ydzierma@geophysik.uni-kiel.de)

E. R. Flueh
IFM-GEOMAR and SFB 574, Wischhofstraße 1-3, D-24148 Kiel, Germany

G. E. Alvarado
Área de Amenazas y Auscultación Sísmica y Volcánica, ICE, Apartado 10032-1000, San José, Costa Rica

M. M. Mora
Escuela Centroamericana de Geología, Universidad de Costa Rica, Apartado Postal 214-2060, Ciudad Universitaria Rodrigo Facio, San Pedro de Montes de Oca, San José, Costa Rica

[1] An array of broadband seismometers transecting the Talamanca Range in southern Costa Rica was operated from 2005 until 2007. In combination with data from a short-period network near Quepos in central Costa Rica, this data is analyzed by the receiver function method to image the crustal structure in south-central Costa Rica. Two strong positive signals are seen in the migrated images, interpreted as the Moho (at around 35 km depth) and an intra-crustal discontinuity (15 km depth). A relatively flat crustal and Moho interface underneath the north-east flank of the Talamanca Range can be followed for a lateral distance of about 50 km parallel to the trench, with only slight changes in the overall geometry. Closer to the coast, the topography of the discontinuities shows several features, most notably a deeper Moho underneath the Talamanca Mountain Range and volcanic arc. Under the highest part of the mountain ranges, the Moho reaches a depth of about 50 km, which indicates that the mountain ranges are approximately isostatically compensated. Local deviations from the crustal thickness expected for isostatic equilibrium occur under the active volcanic arc and in south Costa Rica. In the transition region between the active volcanic arc and the Talamanca Range, both the Moho and intracrustal discontinuity appear distorted, possibly related to the southern edge of the active volcanic zone and deformation within the southern part of the Central Costa Rica Deformed Belt. Near the volcanoes Irazu and Turrialba, a shallow converter occurs, correlating with a low-velocity, low-density body seen in tomography and gravimetry. Applying a grid search for the crustal interface depth and vp/vs ratio cannot constrain vp/vs values well, but points to generally low values (<1.7) in the upper crust. This is consistent with quartz-rich rocks forming the mountain range.

Components: 12,000 words, 15 figures, 3 tables.

Keywords: seismology; receiver functions; Costa Rica; crustal structure; Talamanca.

Index Terms: 7240 Seismology: Subduction zones (1207); 7205 Seismology: Continental crust (1219); 8104 Tectonophysics: Continental margins: convergent.

Received 30 October 2009; **Revised** 1 June 2010; **Accepted** 11 June 2010; **Published** 14 August 2010.

Dzierma, Y., M. M. Thorwart, W. Rabbel, E. R. Flueh, G. E. Alvarado, and M. M. Mora (2010), Imaging crustal structure in south central Costa Rica with receiver functions, *Geochem. Geophys. Geosyst.*, *11*, Q08S26, doi:10.1029/2009GC002936.

Theme: Central American Subduction System
Guest Editors: G. Alvarado, K. Hoernle, and E. Silver

1. Introduction

[2] The Central American subduction zone in Costa Rica has been the object of detailed studies by several international research projects, among them the SFB 574 "Volatiles and Fluids in Subduction Zones" (SFB 574) [*SFB 574*, 2003], a joint seismology, geochemistry, geology, and volcanology project investigating the subduction zone structure, processes and volatile turnover.

[3] While the crustal structure in northern and central Costa Rica is well-known thanks to a variety of seismicity, local earthquake tomography and receiver function studies [*Arroyo et al.*, 2009; *DeShon et al.*, 2003; *Dinc*, 2008; *Dinc et al.*, 2010; *Husen et al.*, 2003; *MacKenzie et al.*, 2008; *Protti et al.*, 1995; *Syracuse et al.*, 2008] and active seismic profiles [*Christeson et al.*, 1999; *Sallarès et al.*, 1999], the crustal thickness in southern Costa Rica has not been accurately confirmed. The Talamanca Range is covered by a dense jungle, which has limited the amount of seismic stations and the resolution of previous local and teleseismic earthquake tomography studies [*Colombo et al.*, 1997; *Husen et al.*, 2003; *Sallarès et al.*, 2001]. An active seismic transect was analyzed by *Stavenhagen* [1998] [see also *Stavenhagen et al.*, 1998], giving insight into the seismic velocity structure of the overriding plate and subducting plate, but the position of the Moho - tentatively placed at 38 km depth - could not be well constrained and relied heavily on gravimetric studies and analogy to northern Costa Rica. An accurate knowledge of the crustal thickness and structure is important for volcanological models [e.g., *Carr*, 1984] and the discussion of the formation of the Central American landbridge ("Pacific models" vs. "in situ models" [*Mann et al.*, 2007; *Meschede and Frisch*, 1998, and references therein]). In this paper we present a receiver function analysis of a broadband seismic transect and a short-period network in south and central Costa Rica, imaging the upper plate Moho and an inner-crustal discontinuity.

2. Regional Background

[4] From southern Mexico to Costa Rica, the Cocos Plate subducts along the Middle American Trench underneath the Caribbean Plate and Panama Microplate [*deMets et al.*, 1994]. Southern Costa Rica and Panama are located on the Panama Microplate [*Adamek et al.*, 1988], which is underthrust by the Caribbean Plate at its northern boundary in the North Panama Deformed Belt. The northwestern boundary of the Panama block is situated along a diffuse fault system in central Costa Rica, the Central Costa Rica Deformed Belt (CCRDB) [*Lewis et al.*, 2008; *Marshall et al.*, 2000], located along the onshore continuation of the North Panama Deformed Belt. Underneath Panama and further into South America, the Nazca Plate subducts nearly perpendicularly to the Middle and South American Trench. It is separated from the Cocos Plate by the Cocos-Nazca Spreading Center and the Panama Fracture Zone (Figure 1).

[5] Onshore, the Costa Rican volcanic arc is built on the Chortis Block in the north and the Chorotega Block in central and southern Costa Rica [*Escalante*, 1990; *Linkimer et al.*, 2010]; the boundary between the blocks is still debated. Segments in the Central American volcanic front have been correlated both with geologic transitions in the upper plate or changes in the lower plate morphology [e.g., *Carr*, 1984; *Carr et al.*, 2007]. In particular, the subducting Cocos Plate off Costa Rica itself is morphologically tripartitioned [*von Huene et al.*, 2000] due to the interaction of the Cocos-Nazca Spreading Center with the Galapagos hotspot [*Barckhausen et al.*, 2001]: (1) a smooth segment of igneous oceanic crust created at the East-Pacific-Rise and (farther south) Cocos-Nazca Spreading Center 20–25 Ma ago, (2) a seamount domain of 15–20 Ma old oceanic crust covered 40% by seamounts, and (3) the aseismic Cocos Ridge formed by the action of the Galapagos hotspot. The Cocos Ridge reaches over 20 km thickness at its crest [*Sallarès et al.*, 2003; *Walther*, 2003] and has therefore been taken responsible for the uplift of the Osa Peninsula and

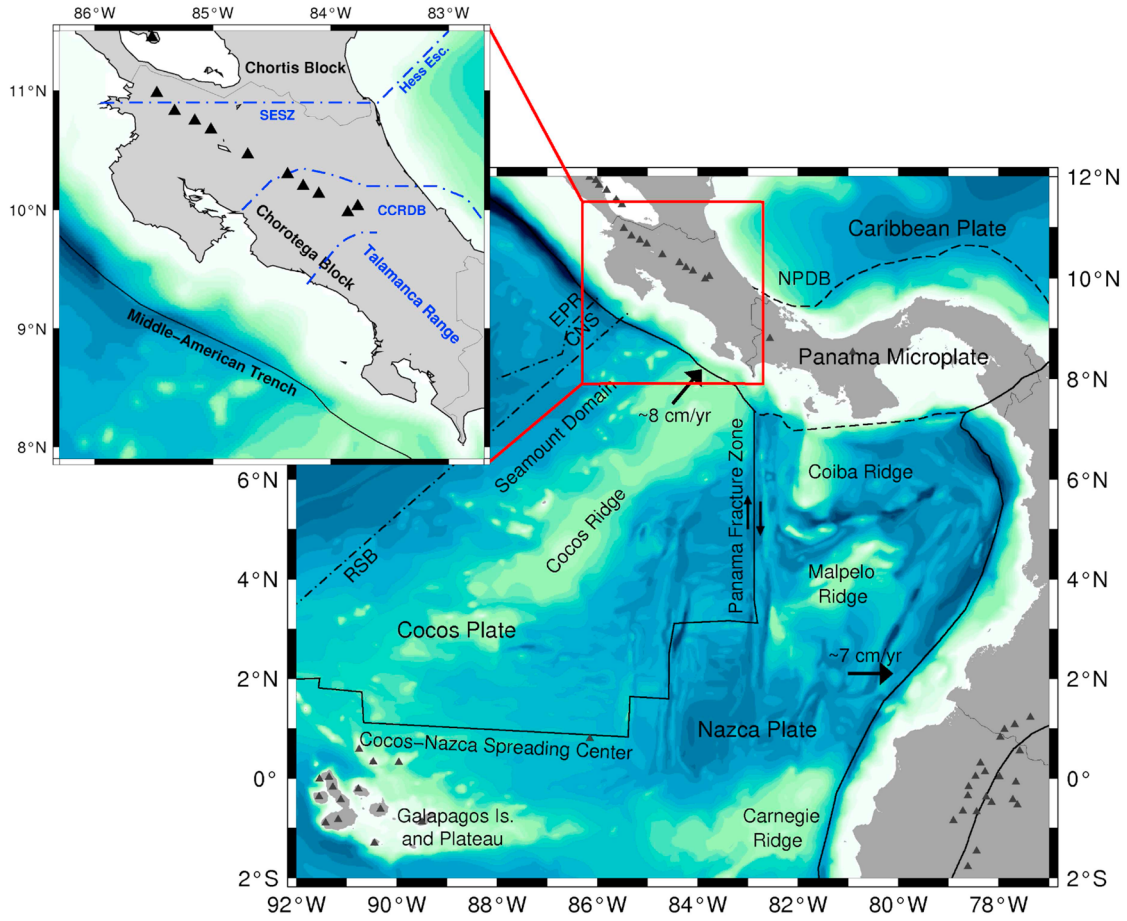

Figure 1. Tectonic overview of southern Central America and the eastern Panama Basin. Volcanoes are indicated by dark triangles. The boundary between crust produced at the East Pacific Rise (EPR) and at the Cocos-Nazca Spreading Center (CNS) is shown schematically. Below is the rough-smooth boundary (RSB), south of which commences the seamount segment. Plate boundaries are based on *Bird* [2003]. The inset shows Costa Rica, with the main fault zones (schematic): the Central Costa Rica Deformed Belt (CCRDB) [*Lewis et al.*, 2008] as a continuation of the North Panama Deformed Belt (NPDB), and the Santa Elena Suture Zone (SESZ) in prolongation of the Hess Escarpment (Hess Esc.) [*Dengo*, 1985; *Barckhausen et al.*, 2001].

Talamanca region [e.g. *LaFemina et al.*, 2009], although the exact timing of the onset of Cocos Ridge collision is still debated.

3. Talamanca Transect and Quepos Network

[6] Sixteen Güralp broadband 3ESP and 3TD seismometers were installed in April 2005 along a transect through the northern Talamanca Range in south central Costa Rica, close to the seismic profile analyzed by *Stavenhagen* [1998]. Three additional land-stations were added in November 2005 to achieve a better coverage of the volcanic chain at the northern end of the transect. To further increase the resolution in this region, two stations were taken out of the southern part of the transect in November/December 2006 and placed north of Turrialba volcano. All stations operated until the end of March 2007 with a sampling rate of 100 Hz. Data from three stations of the ETH Zürich were also included in the analysis (Table 1 and Figure 2).

[7] The Quepos network consisted of 23 ocean bottom seismometers and 15 land stations deployed around the town of Quepos on the Pacific coast of central Costa Rica [*SFB 574*, 2003], used by *Dinc* [2008] together with the Costa Rican permanent network RSN (Red Sísmica Nacional) for a seismicity and tomography study. In the present work, only the land stations have been used (Figure 2 and

Table 1. Coordinates of the Talamanca Transect Stations and ETH Zürich Stations Included in the Analysis and Number of Receiver Functions Analyzed per Station

Station Number	Station Name	Latitude	Longitude	Height (m)	Number of RF
crt-02	Dominical	09°15.972	−83°51.547	0	68
crt-03	Tres Ríos	09°17.947	−83°48.311	415	23
crt-04	Alto San Juan	09°20.021	−83°44.131	828	76
crt-05	Miravalles	09°24.946	−83°40.747	1014	97
crt-06	San José de Rivas	09°26.687	−83°38.189	1205	48
crt-07	Los Ángeles	09°27.526	−83°35.095	1479	169
crt-08	Río Blanco	09°29.912	−83°36.733	1758	48
crt-11	Pejibaye	09°47.934	−83°41.906	728	113
crt-13	San Antonio Arriba	09°47.846	−83°33.740	1038	84
crt-14	Guineal	09°50.282	−83°31.743	955	184
crt-15	Moravia	09°48.878	−83°27.776	1223	159
crt-21	Río Orosi	09°46.376	−83°47.378	1572	165
crt-23	Jaular	09°39.682	−83°52.000	2398	123
crt-25	Alaska	09°31.279	−83°39.790	1585	170
crt-26	Cimarrones	10°04.777	−83°25.908	225	11
crt-27	Tres Equis	09°57.287	−83°33.645	613	113
crt-31	Guápiles	10°07.100	−83°48.650	700	44
crt-32	Guayabo Arriba	09°59.156	−83°43.228	1602	52
crt-33	La Esperanza	10°14.744	−83°56.036	1000	11
crt-34	Virgen del Socorro	10°16.020	−84°09.930	1642	19
Li	Limón	09°59.765	−83°05.657	29	13
Po	Poás	10°10.504	−84°14.932	2493	9
Qu	Quepos	09°23.512	−84°07.436	55	74

Table 2). These were installed in October 2002 and removed in March 2003. Since the network consisted of short-period Mark L4 three-component 1 Hz sensors, only relatively shallow structure down to about Moho depth can be resolved with the receiver functions based on this data; deeper structure would require lower-frequency records.

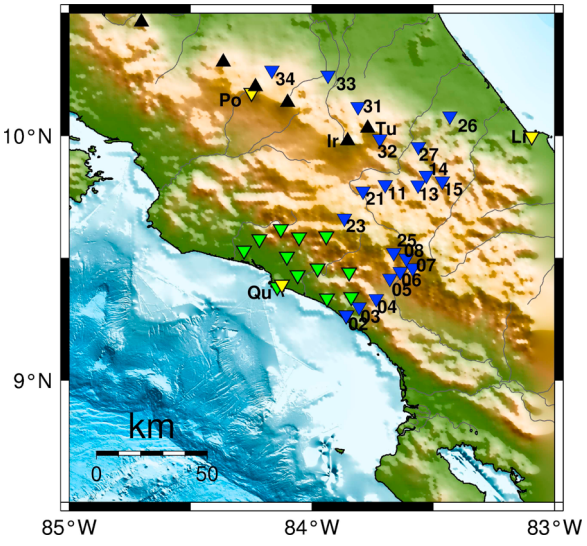

Figure 2. Talamanca Transect stations (blue), Quepos stations (green) and ETH Zürich stations (yellow) included in the analysis. Black triangles denote the principal volcanoes. Irazu (Ir) and Turrialba (Tu) mark the southern end of the volcanic chain in Costa Rica.

4. Methods

4.1. Receiver Function Calculation

[8] The receiver function technique belongs to the standard seismological methods for the investigation of crustal and mantle structure [e.g., *Bostock and*

Table 2. Coordinates of the Quepos Network Land-Stations Included in the Analysis and Number of Receiver Functions per Station

Station Code	Latitude	Longitude	Height (m)	Number of RF
con	09°35.12	−84°03.20	1350	7
cts	09°30.36	−84°06.20	66	6
dom	09°15.94	−83°51.55	44	15
gua	09°20.47	−83°50.32	168	2
man	09°22.89	−84°08.57	41	2
mat	09°20.05	−83°56.32	156	6
nar	09°35.32	−83°56.48	1622	13
rse	09°34.64	−84°13.03	156	10
sav	09°27.48	−83°58.57	193	6
sbl	09°25.80	−84°03.56	65	8
scy	09°37.09	−84°07.72	1471	12
sva	09°26.51	−83°50.80	736	12
pro	09°33.37	−83°51.65	1828	0
vue	09°31.87	−84°16.78	38	1

Rondenay, 1999; *Jones and Phinney*, 1998; *Kind et al.*, 1995, and references therein]. In its most widely applied form, it is based on the fact that seismic P waves can be converted into S waves at discontinuities along the ray path.

[9] The processing steps used in this work follow the procedure outlined, e.g., by *Gossler et al.* [1999]. The selection of teleseismic events for the analysis was based on the following criteria:

[10] 1. P phases: epicentral distance 30° to 95°, magnitude ≥ 5.5.

[11] 2. PP phases: epicentral distance 60° to 180°, magnitude ≥ 6.0.

[12] 3. PKP phases: epicentral distance above 145°, magnitude ≥ 6.0.

[13] The seismogram traces were cut 10 s before and 60 s after the predicted onset and detrended. After restitution of the traces to remove the seismometer characteristics, the traces were band-passed between 0.05 Hz and 5 Hz for the further analysis, and marine noise was filtered out where necessary.

[14] The traces were then rotated by back-azimuth and angle of incidence into the ray coordinate frame (usually denoted L, Q, T), so that the main P wave energy is on the L component, while the P-to-SV converted wave appears on the Q component. Deconvolution of the Q component with the L component removes the source and propagation effects common to both components. We use water-level deconvolution in the frequency domain [*Ammon*, 1991; *Owens et al.*, 1984], smoothed with a Gaussian filter:

$$RF(\omega) = \frac{L^*(\omega)Q(\omega)}{\max\left(L^*(\omega)L(\omega), c\right)} G(\omega) \quad (1)$$

where ω is the frequency, $G(\omega) = \exp\left(-\frac{\omega^2}{4a^2}\right)$ the Gaussian filter with parameter a, and $c = w_l * \max(L^*(\omega)L(\omega))$, with the "water level" w_l. The time domain transformation of $RF(\omega)$

$$rf(t) = \int RF(\omega)\exp(i\omega t)d\omega \quad (2)$$

is called the receiver function. Ideally, it contains only the direct conversions at the discontinuities under the recording stations and their multiples.

[15] The time difference between the P and converted S wave arrival at the surface depends on the depth of the discontinuity where conversion occurred, the difference between the P and S wave velocities vp, vs and the ray parameter p [*Cassidy*, 1992; *Ryberg and Weber*, 2000]. The effect of ray parameter is referred to as normal moveout (NMO) and must be corrected before traces with different ray paths can be compared or stacked for noise reduction. NMO correction is performed to convert all traces to a reference slowness of 6.4s /° so that direct conversions are aligned. Since moveout is different for multiples, they are not aligned after NMO correction, which allows to distinguish between multiples and direct conversions.

4.2. Quality Control and Ray Coverage

[16] After rotation, the signal-to-noise ratio (SNR) on the L component was calculated; traces with SNR between 1.4 and 2. were visually quality-checked; those traces where no clear onset could be discerned were discarded.

[17] A database of 322 teleseismic events was used for the receiver function analysis of the Talamanca Transect and ETH Zürich stations, plus 39 events for the Quepos network. Out of the original 4414 traces, more than half were discarded due to poor quality, resulting in 1777 receiver functions for the Talamanca Transect plus 96 from the ETH Zürich stations and 100 for the Quepos network (Tables 1 and 2).

[18] Most events were located either to the northwest (Alaska-Aleutian subduction zone) or to the southeast (Chilean margin). Some PP and PKP phases could be included to reduce the azimuthal gap (Figure 3).

[19] The area and density of ray coverage can be visualized by plotting the piercing points (Figure 4). For any depth slice in the subsurface, these are the locations where the rays pierce the horizontal; that is, they are where the conversions would occur if they happened at that given depth. Due to the spread-out of the rays underneath each station, the latitudinal coverage of the network increases with depth; conversely, with an increasing area sampled, the density of the rays decreases. Overlap between piercing points of different stations indicates that the results are reliable in the sense that they are not only derived from a single recording site. By using both the Talamanca transect and Quepos stations, good coverage of the area is achieved.

[20] For the Quepos stations, only about a dozen traces are available for each station, so we confine the analysis to the stacked traces and to the inclu-

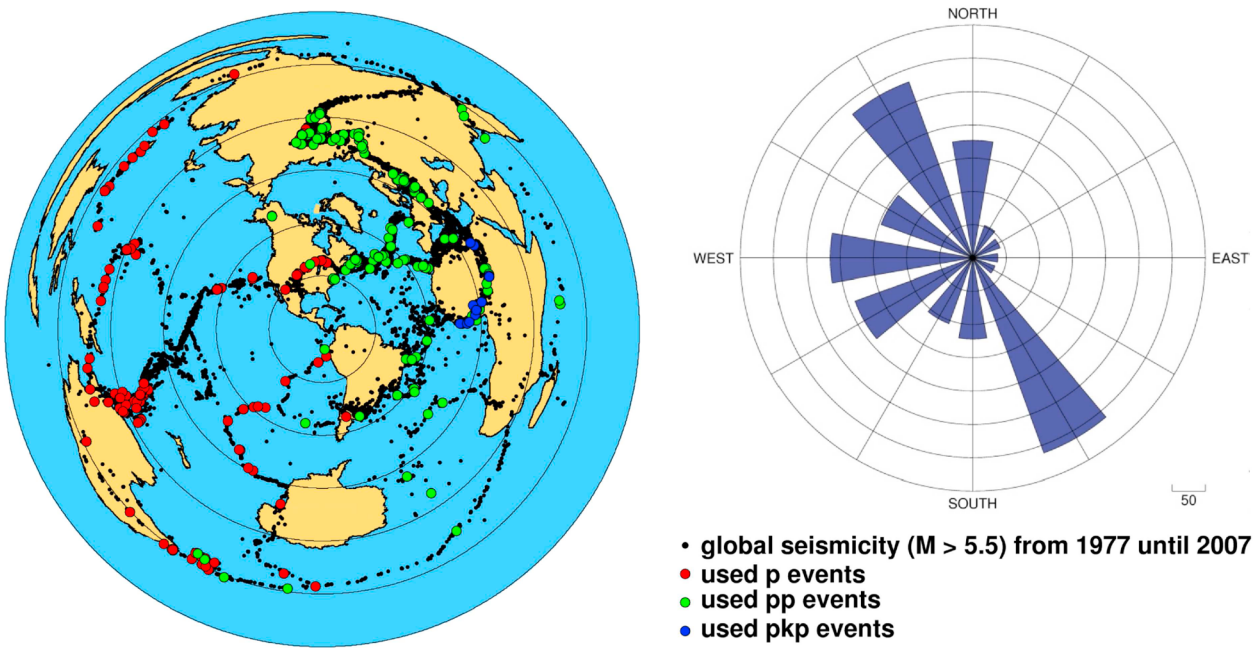

Figure 3. (left) Events used in the receiver function analysis. P phases are displayed in red, PP phases in green, PKP phases in blue. For comparison, the global seismicity over a 30 year period is also plotted. Grid lines are plotted at 30° intervals. (right) Azimuthal distribution of receiver function traces, plotted as a polar histogram.

sion of the Quepos traces in the depth migration (see section 4.4). Although there are too few traces to base a sound analysis on the Quepos stations alone, in combination with the transect stations, they are very useful in filling the gap where the transect jumps northward.

4.3. Resolution

[21] The deconvolution quality and vertical resolution capability of the receiver functions can be assessed from the deconvolution spike on the L component (after deconvolution with itself), the so-called "averaging function". Ideally, this would result in a spike at time 0 (P wave arrival); in the real case, the inclusion of the Gaussian filter in the deconvolution step creates a Gaussian peak. This agrees with the general practice of low-pass filtering receiver functions for display. As a compromise between resolution and noise-suppression, a Gaussian pulse with a width of 1 s was chosen. This limits the vertical resolution of the receiver functions to about 4 km in the midcrust and about 5 km at a depth of around 30 km.

[22] The horizontal resolution of receiver functions is limited by the first Fresnel zone: two structures which fall inside the Fresnel zone cannot be distinguished from another. Calculating with a typical frequency of 1 Hz as above and a maximum S wave speed of about 4 km/s in the crust and upper mantle, the horizontal resolution at 30 km depth is about 12 km, decreasing to 6 km at about 10 km depth.

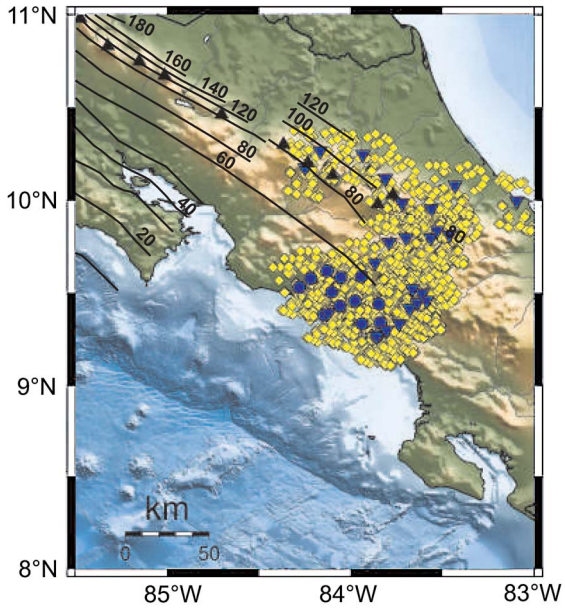

Figure 4. Piercing points (yellow) for both the Talamanca transect, ETH Zürich and Quepos stations (blue symbols) at 35 km depth. Slab contours from *DeShon et al.* [2003] and *Protti et al.* [1995].

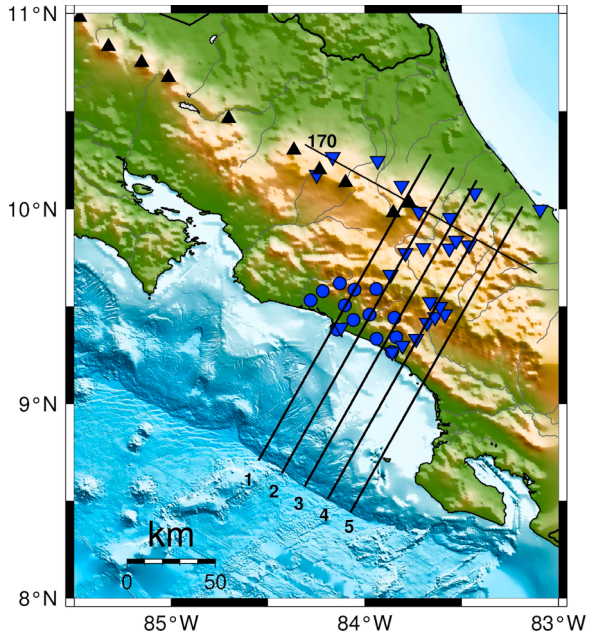

Figure 5. Map of receiver function profiles through the migration volume. Profiles 1–5 start approximately at the trench and run normal to the trench (about N30E) for 200 km. The spacing between these profiles is 45 km. Profile 170 is approximately trench-parallel, at a distance of 170 km from the trench.

4.4. Prestack Depth Migration

[23] In the case of possible dipping structures or azimuthal variation of the receiver functions, stacking smears the results from all individual traces and therefore cannot give a good picture of the real subsurface structures [*Cassidy*, 1992; *Savage*, 1998; *Schlindwein*, 2001]. To tackle possible azimuthal variability and investigate the 3D structure of the discontinuities, 3D prestack depth migration is performed to transfer the seismic traces from the time domain into the depth domain.

[24] The standard migration algorithm used in receiver function studies is based on ray-tracing [*Gossler et al.*, 1999; *Jones and Phinney*, 1998; *Yamauchi et al.*, 2003; *Yuan et al.*, 2000]. Each ray is traced back into the subsurface, so that each recording time (sample) can be associated with a given 3D location (depth, latitude, longitude), which is then assigned the signal amplitude of the receiver function at this time. The subsurface volume traversed by the rays is gridded into cells of 0.1° × 0.1° × 1 km, with neighboring grid cells overlapping by 0.01° and 0.1 km, respectively. The amplitudes of all rays crossing the grid cell are weighted with the amplitude of the deconvolution spike on their L trace and averaged. This creates a volume of signal amplitudes; then several vertical slices are cut through the volume to be displayed as receiver function profiles through the area covered by the seismic stations. For each profile (Figure 5), the values from grid cells within a thin layer around the profile plane are projected onto the surface and averaged (weighted moving average) with a 7 km wide Gaussian filter. The final horizontal resolution achieved is hence limited by the Gaussian filter of 7 km width in addition to the intrinsic resolution capability explained in section 4.3.

[25] A small error is introduced by using a 1D velocity model; however, the technique has been routinely applied in many receiver function studies with good results [e.g., *Gossler et al.*, 1999; *Kosarev et al.*, 1999; *Ramesh et al.*, 2005; *Yuan et al.*, 2000]. Indeed, most studies rely on global Earth models, while still giving good imaging results; but since a 1D regional velocity model for Costa Rica is available, this model by *Quintero and Kissling* [2001] has been used in the calculations presented here. To check for stability of the migration results as a function of the migration velocity model, the analysis was repeated with different models, such as a simple two-layered crust model and an approximation of the *Stavenhagen* [1998] model, which may be more appropriate for southern Costa Rica (but possibly not for central Costa Rica). For all migration velocity models, the results are similar to within a few kilometers, with differences of the order of magnitude of the vertical resolution limit (section 4.3). In particular, the structures imaged with the *Quintero and Kissling* [2001] model and those imaged using the *Stavenhagen* [1998] model are nearly identical, apart from a constant depth offset of about 2–3 km at crustal and up to 5–8 km at Moho depths.

[26] To determine the ray coverage in the grid cells, each cell is assigned a weight based on the sum of the weights of each individual ray (the amplitude of the deconvolution spike). This weight hence depends both on the number of rays crossing the cell and their quality. In the migrated profiles, cells with good ray coverage have a weight 10–100% of the maximum weight achieved by the best-covered grid cell. They are transversed by at least about 30 rays each.

4.5. Semblance Analysis

[27] *Zhu and Kanamori* [2000] introduced a grid-search approach to jointly determine both the Moho depth and crustal vp/vs, based on the arrival times of the primary conversion and first-order multiples

PpPs and PpSs+PsPs and on the assumption of a simple one-layer crust. This algorithm makes use of the fact that the ambiguity in determining conversion depth and vp/vs for the P-to-S converted wave is resolved by the inclusion of the multiples. In this method, an average crustal velocity must be assumed, and weights assigned to the primary conversion and the multiples. A stacking procedure sums the weighted amplitudes of the receiver functions at the Ps, PpPs and PpSs+PsPs arrival times predicted for a given crustal thickness and vp/vs. When the "correct" crustal depth and vp/vs are used, the phases sum coherently; that is, the amplitude of the sum is maximized.

[28] Since this method was designed based on the assumption of a single-layer crust, it can be expected to find the shallowest strong discontinuity. We apply this approach to the broadband receiver functions of those transect stations with more than 50 traces, using the implementation of the method by K. Kieling et al. (Receiver function study in northern Sumatra and the Malaysian peninsula, submitted to *Journal of Seismology*, 2010). Similar to *Eaton et al.* [2006], this introduces the semblance parameter

$$S(t) = \frac{\left(\sum_{i=1}^{n} rf_i(t)\right)^2}{\sum_{i=1}^{n} \left(rf_i(t)\right)^2} \quad (3)$$

where $rf_i(t)$ is the ith out of the total n receiver function traces. The semblance parameter acts as an additional weighting function which suppresses incoherent noise, so that this algorithm becomes more stable and reliable in the presence of noise.

[29] Several runs of the code were calculated for different smoothing, different weights for the multiples, and different crustal velocity. To approximate a single-layer crust, we have used a moving average of 4 s window length for the semblance analysis, which smoothes the crustal structure sufficiently. A mean crustal velocity of 6.5 km/s was assumed and equal weights were assigned to the signal and multiples. The effect of all three parameters is moderate: similar results are obtained for window lengths of 2–5 s (with best quality and stability for 4 s). The influence of the weights is minor as long as the multiples are not weighted too low: runs with weights 0.5, 0.35, 0.15 and 0.5, 0.25, 0.25 for Ps, PsPs and PpPs+PsPs, respectively, give comparable results within the uncertainties given below. Finally, the choice of mean crustal velocity naturally has some influence on the depth of the discontinuity found: if a mean crustal velocity of 6 km/s instead of 6.5 km/s is used, the discontinuities are consistently placed 2 km higher, but with very little change in the retrieved vp/vs ratios. This variation is comparable to the uncertainty from different runs, and the depth variation is below the resolution capability of the receiver functions as discussed above.

[30] While the depth of the discontinuity is rather well constrained to within a few kilometers, the vp/vs-ratio is less tightly determined (deviations of up to 0.1 between different runs). This is due to the fact that it is hard to identify the multiples: visual inspection of the traces (section 5.1) shows that the multiples are not very clearly defined at least unless migration is performed.

5. Results

5.1. Receiver Functions: Traces

[31] An example of the individual receiver functions and their resulting stacked trace is shown in Figure 6. Station crt-23 is typical for what is usually seen: a Moho signal around 3.5 s delay time and crustal signal around 1.5 s, both as coherent positive conversions which can be identified in a large part of the single traces, although with slight azimuthal variation possibly caused by 3D structure of the subsurface. Within a limited range of back-azimuths (e.g., 180°), however, the signals are extremely coherent, showing that these signals cannot be attributed to noise effects.

[32] At station crt-02, a marked negative signal at 0.5–1 s is followed by a very broad positive signal between 3 and 4 s delay time. This station is located at the Pacific coast of Costa Rica, and in this region the subducting Cocos Plate as seen by *Stavenhagen et al.* [1998] and *DeShon et al.* [2003] should be at a depth of around 25–35 km. It is therefore probable that the positive conversion here should be caused by the subducting Cocos Plate rather than the Moho, or jointly image both structures. For the same reason, the features seen at crt-04 are equally complicated. It appears that there is a crustal discontinuity at about 1.5 s delay time, indicated by a positive coherent conversion. As for the positive feature at 3.5 s, this may be the Moho or the subducting plate: at this distance from the trench, active seismic actually finds both at similar depths of about 35 km [*Stavenhagen*, 1998]. For larger distances from the trench, the slab has not been imaged yet and its location is hence unknown. However, it can be expected to be deeper than the Moho, so the positive conversion at 3.5–4. s can be interpreted in terms of the overriding plate Moho.

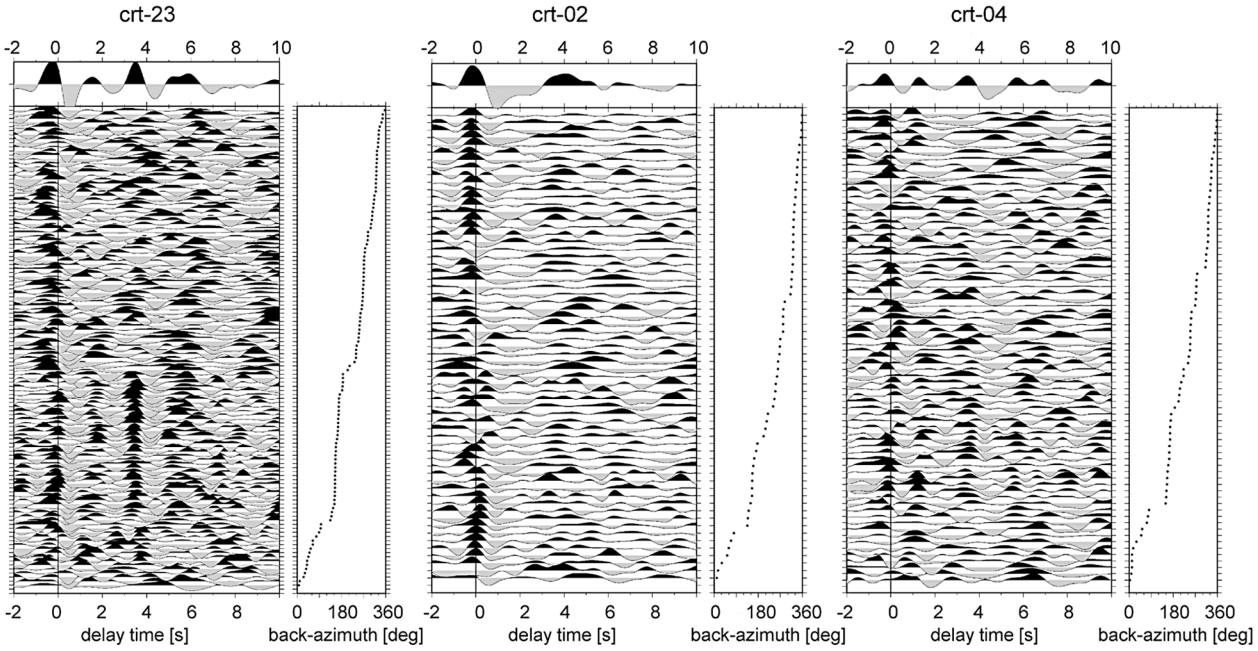

Figure 6. Individual receiver functions for stations (left) crt-23, (middle) crt-02, and (right) crt-04 after NMO-correction, sorted by back-azimuth, and stacked traces (top).

[33] The initial stacks are of limited use due to the strong azimuthal dependencies noted in the individual receiver functions, especially near the trench where we expect dipping structures. Figure 7 shows the stacked traces, ordered by distance from the trench. Close to the coastline (stations MAN, DOM, crt-02, SBL, crt-03 and possibly farther on), a dipping positive signal is seen at 3–6 s delay time, which includes the positive conversion at 3–4 s at station crt-02, already mentioned. This may be the subducting Cocos Plate, which has been imaged by active seismic, seismicity and tomography at this depth. Above, the positive conversion may be interpreted as an inner-crustal discontinuity of the overriding plate, in accordance with active seismic. Further away from the coastline, the Moho is seen at around 3–4 s, with an inner-crustal positive converter around 1–2 s. However, it is hard to interpret the stacked traces without insight into the azimuthal behavior, which may produce smearing/doubling of certain features in the stack. Therefore, we address the problem of azimuthal variability by 3D prestack depth migration.

5.2. Depth Migration

[34] As a help in the interpretation of the observed signals, the seismicity recorded by the Quepos and RSN network is overlain on the migrated receiver function profiles (Figure 8). The location was performed by *Dinc* [2008] in a tomography study. The errors in the hypocenter locations from *Dinc* [2008] were less than 2 km in the horizontal directions and less than 5 km in depth. Since the Quepos network was located in central Costa Rica, no reliable earthquake locations are available for the southern profile. Close to the trench, the position of the subducting Cocos Plate from *Stavenhagen* [1998] and *DeShon et al.* [2003] has been included for orientation, dipping at an angle of about 18° (S). Close to the coastline, the seismicity appears to bend towards somewhat steeper subduction angles (S1).

[35] In all migrated profiles, the Moho is seen as a prominent positive conversion around 35 km depth (M). It appears at about the same depth in all the profiles and is nearly horizontal. Above, there is a second positive conversion at ca. 15 km depth, which is interpreted as an inner-crustal velocity discontinuity (C). The two features are distinctly imaged in the northeastern parts of the profiles, starting at about 140–150 km distance from the trench, and are confirmed by the bootstrap test (section 6.1). The multiples of the crustal discontinuity are observed at 60–70 km depth, as is confirmed by forward modeling (section 6.2). The depth of the crustal interface and Moho retrieved from the forward model agree with the input depths, and can be resolved well by the station geometry.

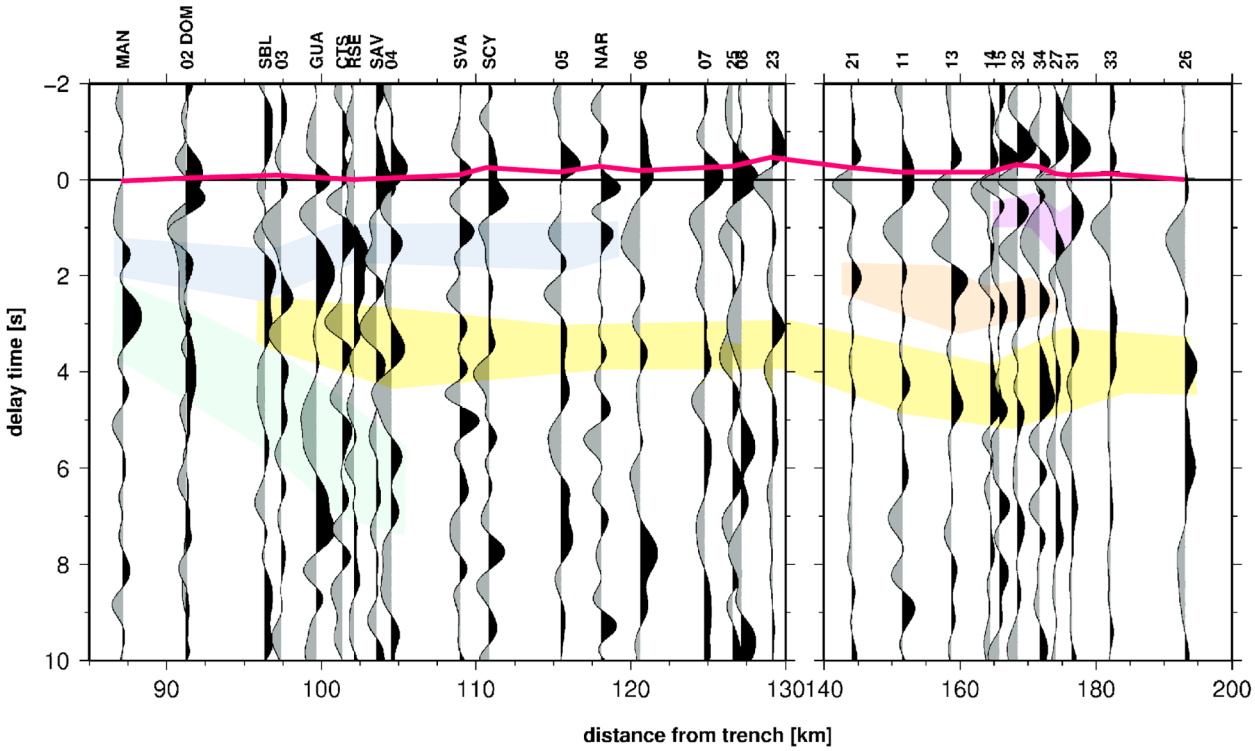

Figure 7. Stacked traces of both the Transect and Quepos receiver functions, ordered by distance from the trench. The stations MAN, DOM and crt-02 are located at the coast. The projection is on a line orthogonal to the trench, similar to profiles 1–5 in Figure 8. The red line gives the "real" zero time of each receiver function trace. Stations with a higher elevation have been plotted starting "earlier"; i.e. the red line has been shifted from the time axis zero, which counts delay time starting at sea level to give a consistent picture of the subsurface beneath the stations. In the way, the time axis can be taken to represent real subsurface depth. Some conspicuous features are colored: a crustal converter at 1–2 s delay time close to the coast (blue), which then becomes hard to follow until at distances of 140–180 km from the trench, where a very shallow crustal conversion (purple, 0.5–1 s) and a deeper feature (orange, 2–3 s) reappear. At 3–4 s delay time, a positive feature, probably the Moho, is seen in most stacked traces (yellow), although it is more clearly identified in the single traces (Figure 6). Very close to the trench, green shading indicates where the slab based on seismicity would be expected. Positive signals are seen on the broadband stations, while the Quepos stations cannot well image this depth.

[36] In the northernmost profile 1 (and to some degree in profile 2), the crustal discontinuity under the mountain range appears to warp up under the mountains (C1), then again go down to 20 km (C2) before again rising somewhat near the coastline (C3). The Moho signal in this profile does not present the very smooth horizontal structure observed farther south, but seems to be depressed below the peak of the mountains (M1).

[37] In the central and southern profiles, the continuation of the crustal interface close to the coastline is unclear. Here a deeper positive signal (about 30 km depth) imaged under the coastline (ca. 100 km distance from trench) appears to bend upwards (D), following to some degree the seismicity which rises towards the volcanic arc at an angle of about 40°. In contrast, the northern profiles show no such correlation of the receiver function images with the seismicity: rather, the seismicity appears to "cross" the structures imaged in the receiver functions, which show a crustal interface (C3) and a disrupted, but rather dipping Moho/slab signal at 100–130 km distance from the trench (MS). The interpretation of these features is difficult, particularly since the receiver functions cannot well resolve small-scale structures. This tectonically complicated region could also not be well resolved by the active seismic study of *Stavenhagen et al.* [1998]. It is possible that the Moho appears as a negative conversion for those stations where the subducting plate is directly underneath the Moho: This would create a velocity inversion and result in a negative polarity conversion at the Moho (a similar effect was observed in the Aegean subduction zone by *Sodoudi* [2005]).

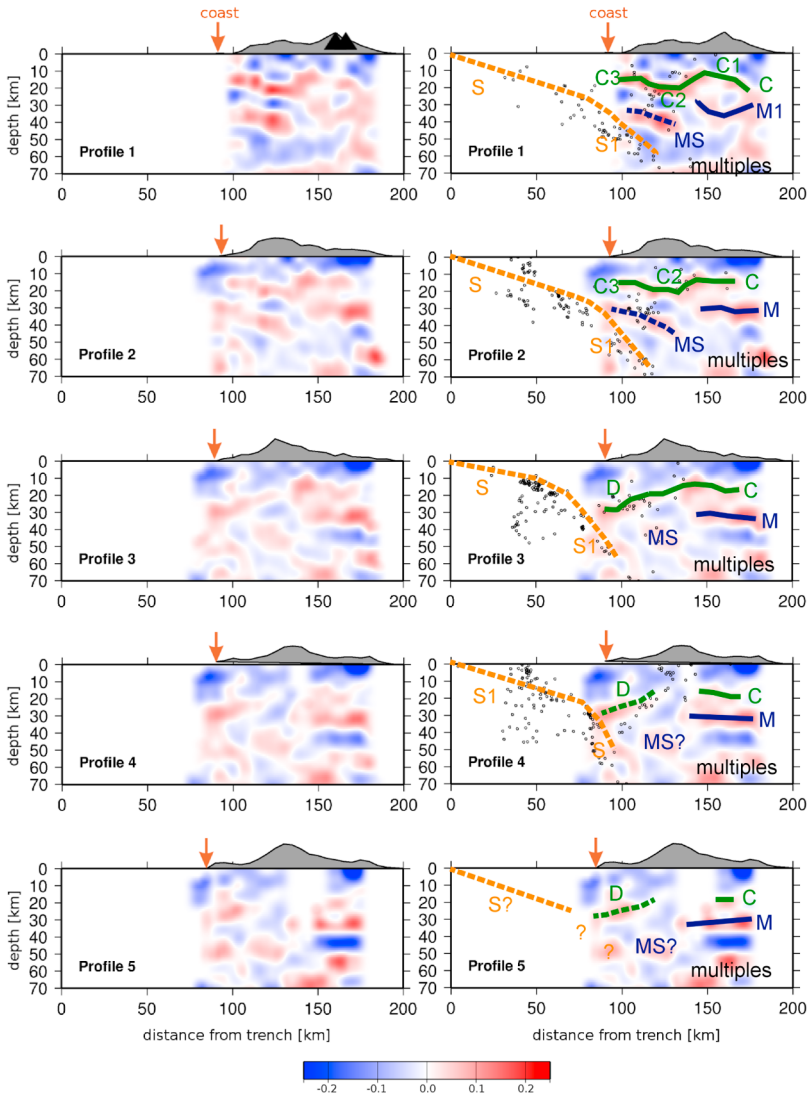

Figure 8. (left) Trench-normal receiver function profiles through the migration volume. Depth and distance from the trench are both in km (to scale). Red amplitudes denote positive conversions, blue amplitudes negative conversions (color scale gives normalized amplitudes). All profiles start at the trench (km 0). The topography is overlain in grey, with amplification factor 4. Black triangles mark the position of the volcanoes Irazu and Turrialba. (right) Annotated version of the profiles, with Quepos and RSN seismicity overlain. M: Moho, M1: deformed Moho, S: slab, S1: possible continuation of slab signal, MS: unclear slab or Moho signal, C, C1, C2, C3: crustal interface, D: dipping crustal interface close to trench.

[38] A trench-parallel section through the migration volume was calculated in the same way as the trench-normal profiles (Figure 9), located at 170 km distance from the trench. Like in the trench-normal profiles, the inner-crustal discontinuity around 15 km depth and the Moho at about 35 km depth are clearly imaged in the trench-parallel profile. Under the Talamanca Range, the Moho shows no large variation in depth. Both the Moho and crustal discontinuity have rather uniform topography over several tens of kilometers into the Talamanca. This picture changes close to the end of the active volcanic chain, where both the Moho and crustal discontinuity are disrupted. Two jumps/breaks in the continuous structures are evident, at about 70 km and 90 km along the trench, respectively. The breaks coincide spatially with the end of the Talamanca Range, the edge of the active volcanic arc and the southern end of the broad CCRDB.

[39] Under Irazu and Turrialba volcanoes, a shallow positive conversion close to the surface is underlain

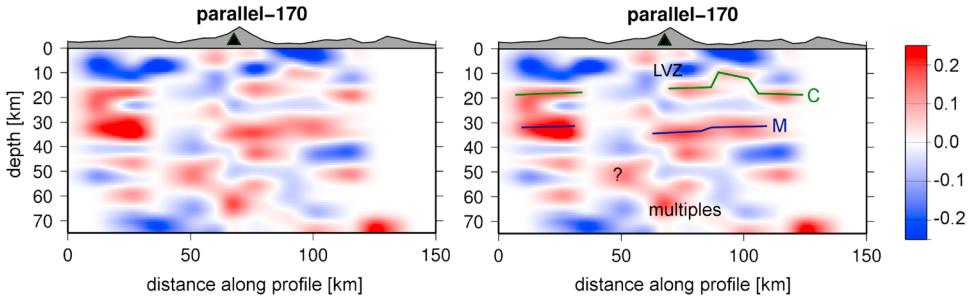

Figure 9. (left) Trench-parallel receiver function profile through the migration volume, at 170 km distance from the trench. The topography (exaggerated by a factor 4) is shown in grey, where black triangles mark active volcanoes. Distance along the trench increases southwards. (right) Annotated version. The profile illustrates the lateral variations in crustal (C) and Moho (M) structure, and shows the low-velocity zone beneath Irazú volcano. The color scale gives the normalized amplitude of the conversions. Profile 1 cuts through the parallel profile at distance 80 km along the profile.

by a negative conversion at 5–10 km depth. This may be an indication of a low-velocity zone under the active volcanoes Irazu and Turrialba.

5.3. Estimation of vp/vs

[40] Satisfactory results in the semblance analysis are obtained for some stations with a sufficient number of traces and located sufficiently far in-land (crt-11, crt-13, crt-27, and crt-32, Table 3 and Figure 10). An interface depth of 15–22 km is found at all four stations, corresponding to the depth of the crustal discontinuity.

[41] While the uncertainty in vp/vs is very large, we do find consistently low values in the range 1.5–1.7 for the upper crust. Although values of 1.5–1.6 are not physically reasonable, the results still point to very low vp/vs ratios considerably below the "standard" value for a Poisson solid of 1.73. Low vp/vs can be expected for the intermediate to felsic crystalline upper crust of the mountain range [*de Boer et al.*, 1995; *Gräfe*, 1998; *Kussmaul*, 2000], as quartz-rich rocks have particularly low vp/vs ratios, and values as low as 1.62 have been proposed [*Linkimer et al.*, 2010].

6. Stability of Results

6.1. Bootstrap Test

[42] The bootstrap method is a statistical test for the stability of the results [*Efron and Tibshirani*,

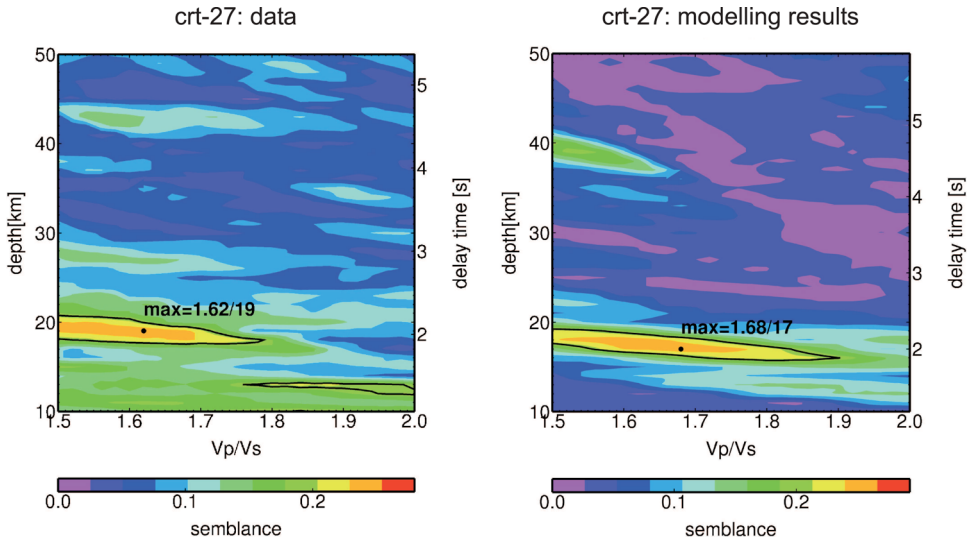

Figure 10. Example for semblance matrix obtained with the Zhu-Kanamori algorithm for station crt-27. (left) Semblance matrix calculated from the data. The maximum semblance is found for a crustal interface depth of 19 km and vp/vs ≈ 1.62. The contour line is drawn at 75% maximum semblance. (right) Example obtained for synthetic data with signal-to-noise ratio 1.5, an interface depth of 17 km and vp/vs = 1.6 in the upper crust.

Table 3. Results From the *Zhu and Kanamori* [2000] Analysis

Station Code	Interface Depth (km)	vp/vs
crt-11	21 ± 3	1.65 ± 0.1
crt-13	22 ± 3	1.50 −1.62
crt-27	19 ± 3	1.52 −1.62
crt-32	15 ± 3	1.62 −1.70

1986]. We have implemented it such that the processing and migration is performed for two random, non-overlapping subsets of the data (even vs. odd event numbers). The results for both data sets are compared to see which features are reliable, and the variations between the sets can be taken as an estimate of the uncertainties in the observed discontinuities.

[43] For the migrated profiles, profile 3 evidently achieves best results in the bootstrap test (Figure 11) because of the best ray coverage; profile 2 is shown as a example for the average data quality and profile 5 for the worst network coverage. The bootstrap test confirms the major features identified in the migrated profiles, and the deviations in the depth of converted signals are smaller than the depth resolution (section 4.3).

[44] For the vp/vs analysis the bootstrap test was performed in the same way by again choosing random subsets of half the total size. Only those results are considered which are stable under this test. Maybe not surprisingly, the results for stations close to the Pacific coast are poor, most likely as an effect of the dipping plate interface. The *Zhu and Kanamori* [2000] algorithm is not designed to include dipping features and cannot be applied where azimuthal effects are too strong. We therefore tested each station for possibly diverging results when only 180°-slices of back-azimuth were included. Those stations where considerable changes emerged for different back-azimuth subsets were excluded from the analysis. Some other stations did not give stable results due to the fact that the semblance value retrieved for the Moho and crustal interface was similar. Here, the semblance analysis in some cases (bootstrap runs, parameterizations) retrieved the Moho depth, in others the crustal interface.

[45] We only present results for those four stations that give stable results both under bootstrap and variation of input parameters as explained in Section 4.5, and if confined to particular back-azimuth data subsets. Even at these high-quality stations, the maximum semblance is low, indicating that the data set does not allow a reliable exact determination of both vp/vs and depth. This is probably due to the fact that the structure is considerably more complicated than a simple one-layer

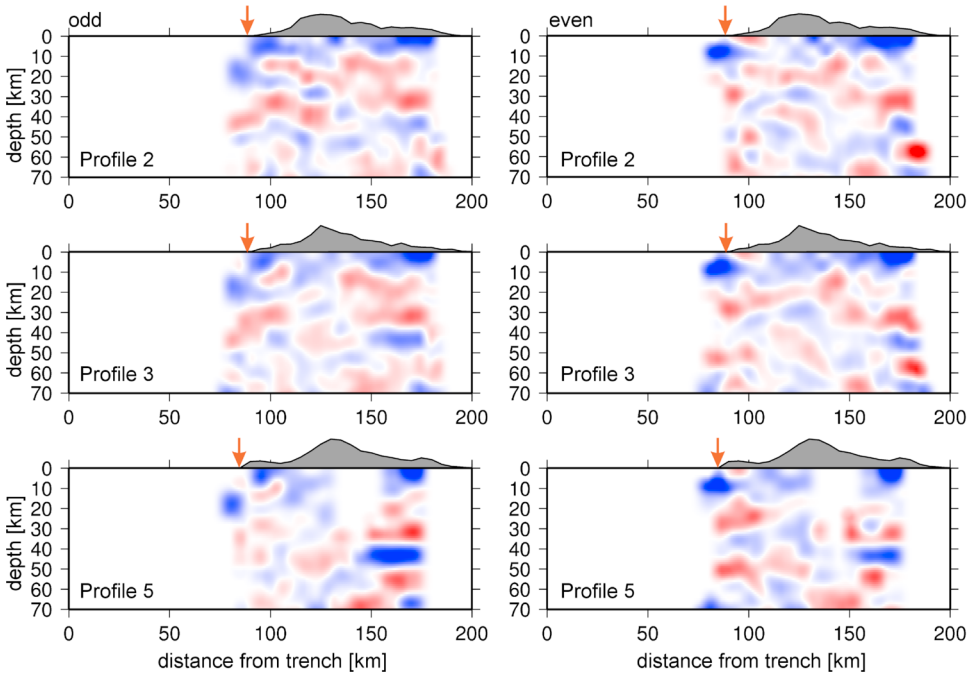

Figure 11. Bootstrap test for migrated receiver function profiles 2, 3 and 5. (left) Migration using odd-numbered traces only. (right) Migration using even-numbered traces.

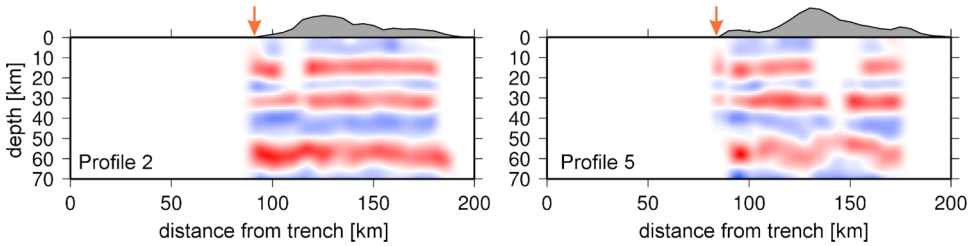

Figure 12. Forward modeling results for a crustal interface at 17 km depth and Moho at 35 km depth. The traces were calculated along the real observation geometry for the events-receiver configuration used in the analysis and signal-to-noise ratio 1.5, and then processed in the same way as the real data. Migration profiles 2 and 5 are displayed to show that even the edge profile 5 can well resolve the structure. The crustal multiple is observed at 60–70 km depth, the Moho multiple occurs at greater depth and is therefore not visible in the migrated image presented.

crust over a half-space, and multiples are hard to identify because of azimuthal effects and possibly deeper structure.

6.2. Forward Modeling

[46] The results were tested for consistency by forward modeling with the algorithm by *Frederiksen and Bostock* [2000]. This serves as a test on the resolution of the network configuration and on the possibility to retrieve the information from the data. Several different forward models were calculated. We show a representative example in which the input model is held very simple, consisting of the following: (1) a 17 km thick upper crust (vp = 6.3 km/s, vs = 3.7 km/s, density ρ = 2700 kg/m^3), (2) a 18 km thick lower crust (vp = 7.2 km/s, vs = 4.1 km/s, ρ = 2900 kg/m^3), and (3) a mantle half-space (vp = 8.0 km/s, vs = 4.57 km/s, ρ = 3300 kg/m^3).

[47] Synthetic traces were created for the actual event-receiver configuration, and incoherent (white) noise was added to the individual traces with a signal-to-noise ratio of 1.5, which is approximately the lowest signal-to-noise ratio of the traces that still passed the quality check and entered the analysis. Processing was done in the same way as the real data, resulting in comparable migrated profiles (Figure 12).

[48] Synthetic modeling for the semblance analysis was performed for different crustal velocities, interface depths and vp/vs ratios, again using a signal-to-noise ratio of 1.5 (example shown in Figure 10 for an input model with interface depth 17 km and vp/vs 1.6). The interface depths were retrieved within 2–3 km and vp/vs within 0.04. However, the broad "bull's eye" around the maximum of the semblance matrix suggests that vp/vs is not well constrained, and an uncertainty of about 0.1 in vp/vs (corresponding to the width of the 75% maximum semblance contour) is more realistic.

7. Discussion

7.1. Large-Scale Structure

[49] The main crustal structure seen in receiver functions is compared with the results from active seismic by *Stavenhagen* [1998] in Figure 13. The surfaces identified in the receiver functions correspond well to the structure observed by active seismic at greater distances from the trench. Both the Moho and the crustal discontinuity are imaged at similar depths where a velocity contrast is observed in the active seismic profile. In particular, this confirms the identification of the Moho around 35 km depth. Closer to the shoreline, discontinuities identified in the receiver functions could not be easily interpreted, a tentative interpretation will be given below. In this region, the velocity model from active seismic is limited in coverage and resolution.

[50] In addition to the active seismic transect, south central Costa Rica has been investigated by several research groups by local earthquake tomography [*Arroyo et al.*, 2009; *Dinc*, 2008; *Husen et al.*, 2003]. Some of the published tomographic depth slices fall inside our investigation area (Figure 14). The receiver functions are sensitive to sharp changes in absolute velocity and can hence be compared with those regions in the tomography image where the velocities change rapidly. The large-scale features like the Moho and crustal discontinuity in the north-eastern part of the profiles (M, C) match well with the velocity contours of *Husen et al.* [2003]. In the northern profile (Figures 14a–14c), the Moho topography close to the coastline was found to have some topography, particularly a 5–10 km bulge-like feature close to the coastline. This same feature

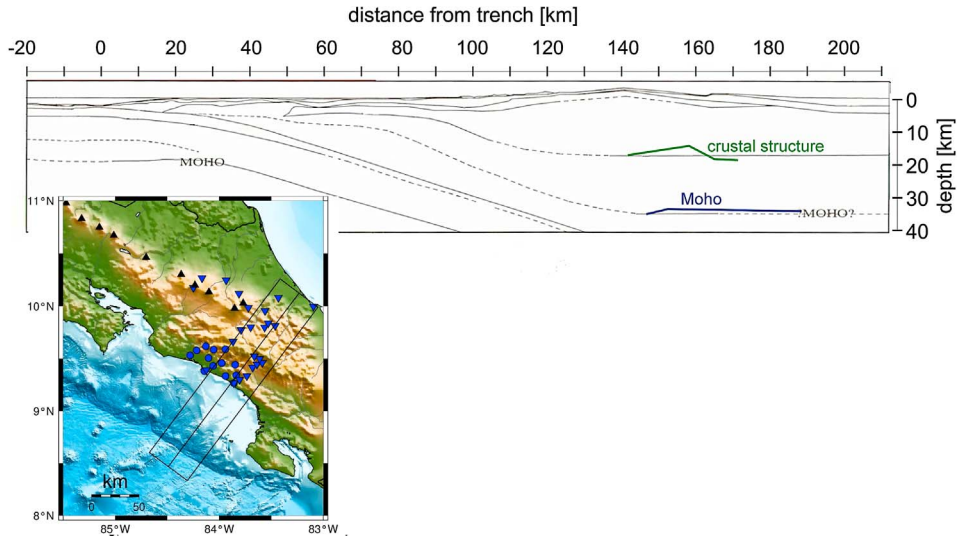

Figure 13. Comparison of receiver function results with active seismic profile by *Stavenhagen* [1998]. Prominent interfaces identified in the receiver function analysis are plotted onto the profile.

is seen in the absolute velocities by *Dinc* [2008] (blue line in Figure 14), and appears in a similar way, although not quite as obvious, in the absolute velocity contours by *Husen et al.* [2003]. The adjacent negative relative velocity anomaly (LVZ) was tentatively interpreted as a subducting seamount by *Husen et al.* [2003].

[51] In the corresponding southern profiles (Figures 14d and 14e), the Moho close to the trench

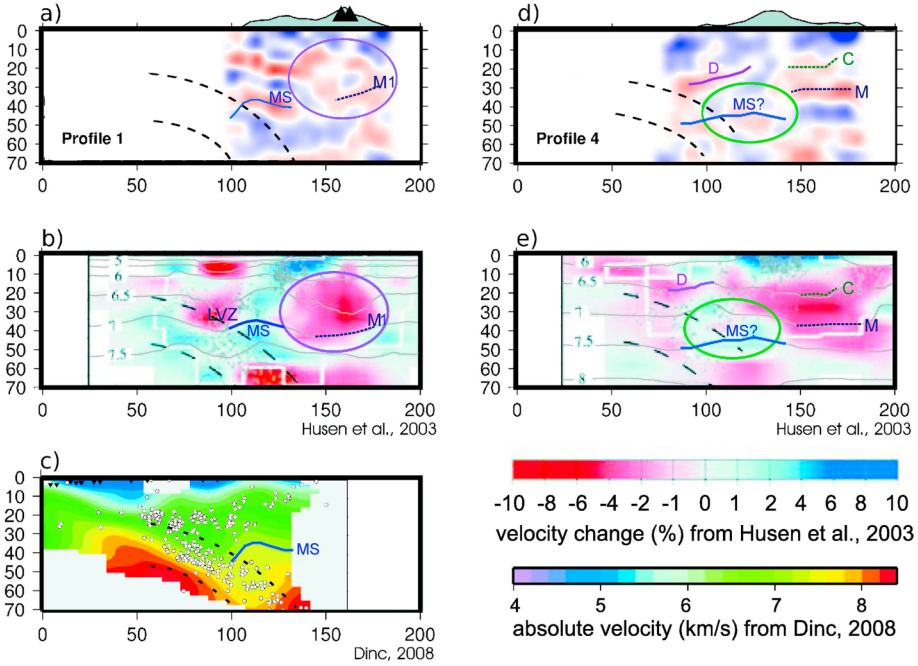

Figure 14. Comparison of (a and d) receiver function results with (b and e) relative velocity anomalies Δvp from tomography by *Husen et al.* [2003] and (c) absolute vp from tomography by *Dinc* [2008]. Figures 14a–14c show profiles approximately along profile 1 in Figure 8; Figures 14d and 14e show those along profile 4. The profiles from tomography studies have been shifted so that all profiles show the same distance from the trench and depth range. The Moho (M) and crustal discontinuity (C) found in the receiver function profile agree with the tomography results. Several other features marked in the profiles (fattened absolute velocity contours, ellipses) are discussed in the text.

could not be clearly identified, but an upward bending feature was instead observed (D). The interpretation of this was unclear based on receiver functions alone. Comparing the receiver function profile 4 with the tomography, it is seen that the tomography image reproduces the upward bending feature to some degree along the 6.5 km/s vp velocity contour, so we interpret it as the continuation of the crustal discontinuity. Farther inland, the velocity contour becomes flat at a depth of about 20 km. This is mirrored in the receiver functions, showing a flat crustal discontinuity at this depth (140–170 km from the trench, C).

[52] The Moho underneath the north-eastern flank of the Talamanca Range (Figure 14, M) is horizontal and with hardly any complicated topography visible at the resolution of the receiver function. This is consistent both with the absolute velocity contours in the tomography and with the structure observed by active seismic. Closer to the trench, the disruption of the Moho signal in receiver functions between 100 and 140 km distance from the trench coincides with a fast velocity anomaly in the tomography image, which underlies the upward bend in the crustal discontinuity discussed above (green ellipse in Figure 14). The interpretation of this feature is difficult, in particular since the tomographic image is smoothed so that rapid variations in structure are smeared. Still, the 7.5 km/s velocity contour reflects to some degree the depth variations of the receiver function conversions.

7.2. Implications of Moho Topography Underneath the Talamanca Range

[53] The fact that the Moho underneath the northeast flank of the Talamanca Range appears at a depth of about 35 km in the receiver functions - a "normal" thickness for continental crust - is compatible with the gravity field as shown by *Stavenhagen* [1998]. However, a constant crustal thickness would be contrary to what might be expected for the highest mountain range of Central America. To be isostatically compensated, this high mountain range would need a substantial crustal root, i.e., a deeper than average Moho.

[54] To check if the Talamanca is in isostatic equilibrium, we have estimated the expected Moho depth for Airy-type isostasy, based on the densities modeled by *Stavenhagen* [1998]:

[55] 1. ρ_{crust} = 2850 kg/m^3 in the crust (the average of the densities of upper and lower crust found by *Stavenhagen* [1998]).

[56] 2. ρ_{mantle} = 3300 kg/m^3 in the upper mantle.

[57] 3. For the mass load above sea level we considered two end-member scenarios: ρ_{topo} = 2400 kg/m^3 for a low-mass scenario vs. 2700 kg/m^3 for the high-mass scenario.

[58] Assuming that the crust should be isostatically compensated far from the Talamanca, the Moho was set to the depth coinciding with the receiver function Moho signal near the Caribbean coast. To account for an uncertainty range, we set the depth in the absence of mass-load to 30 km in the deepest and 25 km in the shallowest scenario. The two cases can be considered the extremes between which the Moho signal should be expected.

[59] The agreement of the estimated isostatically equilibrated Moho depth with the observed Moho signal in the receiver function profiles (Figure 15) is generally good. In particular, the deep signal MS between 40 and 50 km depth (100–130 km distance) which was previously unexplained now appears as a deep Moho underneath the elevated topography. This indicates that indeed the Moho is imaged in the receiver functions even in the region close to the shoreline, where interaction with the subducting plate and ray coverage obscured the active seismic results from *Stavenhagen* [1998]. The Moho in this region is actually downwarped under the weight of the mountain range.

[60] However, some deviations from isostatic compensation appear in profile 1, where the Moho signal under the end of the active volcanic arc (M1) is about 10 km shallower than expected under isostasy. Here, support by upwelling magma and reduced crustal densities may interact to place the Moho at shallower depths than predicted. Alternatively, the presence of a low-velocity zone at these levels in the lower crust (see below) may create a complicated conversion signal which need not coincide exactly with the Moho, but could be the lower edge of the low-velocity zone.

[61] The southern profiles (4 and 5) show a deeper depression (ca. 5 km) of the positive conversion under the peaks of the Talamanca Range (MS), whereas close to the coast (D) it appears shallower. The conversion D gives over farther inland to the crustal interface, so this may include signals both from the crust and Moho conversion. It is equally unclear for these profiles (4, 5) if the positive conversions (MS) can really be identified with the Moho. In particular, the position of the subducting slab in this region is unclear, since the seismicity

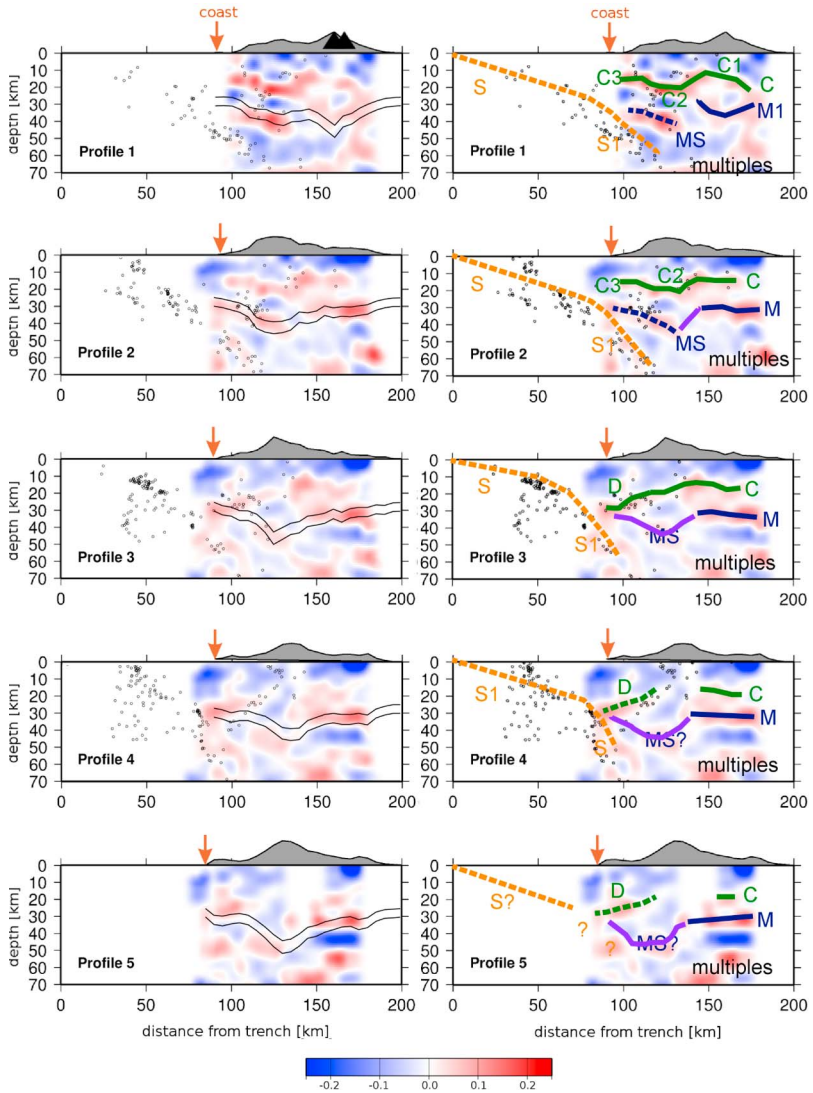

Figure 15. (left) Receiver function profiles from Figure 8 with expected Moho depth for Airy-type isostasy overlain (black lines giving low- and high-mass end-member scenarios). (right) Interpretation as in Figure 8, for comparison. The MS signal is now interpreted as continuation of the Moho as suggested by isostasy.

bends to steeper angles, staying below the positive conversion signal MS. In contrast to this, *Protti et al.* [1995] and *Stavenhagen* [1998] suggest a flatter subducting slab which would coincide with the MS signal. However, the blocky nature of the conversions together with the observed seismicity along distinct lineaments between the blocks suggests that the overriding plate crust may be segmented in this region.

[62] While the interpretation of the isostasy estimation calls for further investigation by modeling studies, the Moho depth predicted for isostatic equilibrium indicates that the previously unexplained conversion MS is probably the Moho of the crustal root beneath the mountain peaks. Apart from local deviations underneath the active volcanic arc and in the coastal region of the Talamanca Range, the crust appears to be close to isostatically compensated. If this is the case, the "original" crustal thickness in the absence of elevated topography would be between 25 and 30 km. This is slightly thinner than "average" continental crust, which is plausible for the "tectonized crust" of the Costa Rican landbridge.

7.3. Structural Break Between the Talamanca and Active Volcanic Arc

[63] The segmentation of the crust of the overriding plate suggested above can also be followed in the trench-parallel profile 170. Northwest of the vol-

canoes Irazu and Turrialba, this profile overlaps with the profile by *MacKenzie et al.* [2008], which shows a similar structure: a thick positive conversion at 15–35 km depth, which may merge both the Moho and crustal interface. This structure remains constant over several tens of kilometers in the *MacKenzie et al.* [2008] profile, but is disrupted at the end of the active volcanic arc under Irazu.

[64] In the transition region between the edge of the active volcanic arc and the Talamanca Range, some disturbance in the crustal and Moho interface appears in the form of a jump in the Moho depth and distorted crustal structure. Since the two volcanoes Irazu and Turrialba are both located inside the broad region of the Central Costa Rica Deformed Belt, the disrupted structures seen in this area may be linked to the faulted and disrupted region of the CCRDB. If this were indeed the case, the receiver functions would indicate that the crust is disrupted down to the Moho level. This is in agreement with the seismicity observed in profiles 3 and 4 (discussed above), which reaches up along the block boundaries observed in the receiver functions. That the CCRDB may reach Moho depths was also suggested to some degree by the tomography study of *Dinc* [2008], who finds both a significant vp and vp/vs contrast along the southern boundary of the CCRDB, reaching down to a depth of 40 km.

7.4. Structure Under the Edge of the Volcanic Chain

[65] A low-velocity anomaly has been imaged by *Husen et al.* [2003] beneath the volcanoes, which coincides closely with the anomalous structure found in receiver functions (Figures 14a–14c and conversions C1, M1 in Figure 15). Its lower boundary gives rise to a positive conversion in the receiver functions, as is expected for a velocity decrease (traveling upwards along the ray). Whether or not this lower boundary coincides with the Moho is unclear; based on the isostasy estimate and the velocity contours from *Husen et al.* [2003], the Moho would be expected underneath the low-velocity zone. The upper boundary of this zone is problematic, due to the limited resolution both of the receiver functions and the tomography and the relatively strong smoothing applied by *Husen et al.* [2003]. The receiver functions are sensitive to sharp changes in absolute velocity, whereas the tomography images relative velocity perturbations in a larger volume. Therefore, not all features can be expected to be imaged in the same way by both methods. A hypothetical magma chamber below the volcanic chain would probably not occur as a first-order feature like a simple ellipsoidal chamber of reduced velocities, but would certainly involve more complicated structure such as dyke and sill-type intrusive interlayering. Whereas the tomography might smooth over fine scale effects and image an effective decrease in vp in a larger region, the receiver functions are more sensitive to the structural features in the magma supply system. That the position of the anomalies imaged by both methods coincides points to the existence of distinct structure beneath the volcanic chain.

[66] At shallow depth of 5–10 km, the trench-parallel profile 170 shows a negative conversion indicating a low-velocity zone beneath the volcanoes. This structure is better resolved by *Arroyo et al.* [2009], who image a very shallow low-velocity anomaly beneath the volcanoes. The location of this zone can be linked with gravimetric observations by *Lücke et al.* [2008], who found a low-density body from gravimetric modeling, interpreted as a joint magma reservoir beneath the volcanoes Irazu and Turrialba at 1–10 km depth. Although their model was a-priori restricted to depths down to 10 km, the low-velocity feature may reach even deeper, as suggested by the comparison of the gravity model with low velocities observed in seismic tomography [*Arroyo et al.*, 2009] that extend to greater depth. This would again be consistent with both the *Husen et al.* [2003] tomography and the receiver functions.

8. Conclusions

[67] The overriding plate Moho and crustal structure in south-central Costa Rica is imaged by a receiver function analysis using 3D prestack depth migration. The Moho of the overriding plate is found at an average depth of 35 km. An inner-crustal discontinuity is imaged at 15 km, in agreement with findings from an active seismic profile [*Stavenhagen*, 1998]. The absolute depth of the discontinuities varies within about 5 km depending which velocity model is assumed for the migration.

[68] The topography of the discontinuities shows several features, most notably a deeper Moho underneath the Talamanca Mountain Range and volcanic arc. Under the highest part of the mountain ranges, the Moho reaches a depth of up to 50 km, which indicates that the mountain ranges are approximately isostatically compensated. Local deviations of 5–10 km from the crustal thickness expected for

isostatic equilibrium occur under the active volcanic arc and in south Costa Rica.

[69] The crustal discontinuity and the Moho can be imaged with little variation across 50 km lateral distance along the trench, but are disrupted in the vicinity of the active volcanic arc. Here the end of the volcanic arc and beginning of the Talamanca Range, together with the broad Central Costa Rica Deformed Belt, may be visible as jumps in the crustal and Moho conversions. In this region, crustal seismicity appears to occur along discrete fault lines reaching from the surface to Moho depths, and changes are observed in vp and vp/vs imaged by tomography [*Dinc*, 2008]. This indicates that the total crust may be disrupted in this region.

[70] A low-velocity zone is found at a shallow depth (around 5–10 km) locally underneath the active volcanoes Irazu and Turrialba. A larger magma-chamber or feeding system may be present underneath, indicated both by anomalous receiver function conversions and tomography [*Husen et al.*, 2003].

[71] Applying a grid search for the crustal interface depth and vp/vs-ratio cannot constrain vp/vs values well, but points to generally low values (<1.7) in the upper crust and confirms the depth of the crustal interface. Low vp/vs values were observed in north Costa Rica by *Linkimer et al.* [2010] and are consistent with quartz-rich rocks forming the mountain range.

Acknowledgments

[72] This is contribution 184 of the SFB 574 "Volatiles and Fluids in Subduction Zones" at the University of Kiel, funded by the German Research Foundation (DFG). We thank the associate editor and two anonymous reviewers for their helpful suggestions, which improved this work significantly. About half of the Talamanca Transect stations and all the Quepos network stations were provided by the GeoForschungsZentrum Potsdam instrument pool. We thank Stephan Husen for the data of the ETH Zürich broadband stations. Xiaohui Yuan provided his codes for the receiver function analysis, which were used for the NMO correction. Katrin Kieling and Frank Krüger, GFZ Potsdam, kindly provided their code for the Zhu and Kanamori algorithm. Kathrin Lieser and Gudrun Reim helped with the preparation of the figures. This research has made use of the SH (Seismic Handler), sac (Seismic Analysis Code), GMT (General Mapping Tool) and Passcal software packages and of NASA's Physics/Astrophics Data System.

References

Adamek, S., C. Frohlich, and W. D. Pennington (1988), Seismicity of the Caribbean-Nazca Plate Boundary: Constraints on microplate tectonics of the Panama region, *J. Geophys. Res.*, *93*(B3), 2053–5075.

Ammon, C. J. (1991), The isolation of receiver effects from teleseismic P waveforms, *Bull. Seismol. Soc. Am.*, *81*(6), 2504–2510.

Arroyo, I. G., S. Husen, E. R. Flueh, J. Gossler, E. Kissling, and G. E. Alvarado (2009), Three-dimensional P-wave velocity structure on the shallow part of the Central Costa Rican Pacific margin from local earthquake tomography using off- and onshore networks, *Geophys. J. Int.*, *179*, 827–849, doi:10.111/j.1365-246X.2009.04342.X.

Barckhausen, U., C. R. Ranero, R. von Huene, S. C. Cande, and H. A. Roeser (2001), Revised tectonic boundaries in the Cocos Plate off Costa Rica: Implications for the segmentation of the convergent margin and for plate tectonic models, *J. Geophys. Res.*, *106*(B9), 19,207–19,220.

Bird, P. (2003), An updated digital model of plate boundaries, *Geochem. Geophys. Geosyst.*, *4*(3), 1027, doi:10.1029/2001GC000252.

Bostock, M. G., and S. Rondenay (1999), Migration of scattered teleseismic body waves, *Geophys. J. Int.*, *137*, 732–746.

Carr, M. J. (1984), Symmetrical and segmented variation of physical and geochemical characteristics of the Central American volcanic front, *J. Volcanol. Geotherm. Res.*, *20*, 231–252.

Carr, M. J., L. C. Patino, and M. D. Feigenson (2007), Petrology and geochemistry of lavas, in *Central America: Geology, Resources and Hazards*, vol. 1, edited by J. Bundschuh and G. E. Alvarado, pp. 565–577, Taylor and Francis, London.

Cassidy, J. F. (1992), Numerical experiments in broadband receiver function analysis, *Bull. Seismol. Soc. Am.*, *82*(3), 1453–1474.

Christeson, G. L., K. D. McIntosh, T. H. Shipley, E. R. Flueh, and H. Goedde (1999), Structure of the Costa Rica convergent margin, offshore Nicoya Peninsula, *J. Geophys. Res.*, *104*(B11), 25,443–25,468.

Colombo, D., G. B. Cimini, and R. de France (1997), Three-dimensional velocity structure of the upper mantle beneath Costa Rica from a teleseismic tomography study, *Geophys. J. Int.*, *131*, 189–208.

de Boer, J. Z., M. S. Drummond, M. J. Bordelon, M. J. Defant, H. Bellon, and R. C. Maury (1995), Cenozoic magmatic phases of the Costa Rican island arc (Cordillera de Talamanca), in *Geologic and Tectonic Development of the Caribbean Plate Boundary in Southern Central America*, edited by P. Mann, *Spec. Pap. Geol. Soc. Am*, 295, 35–56.

deMets, C., R. G. Gordon, D. F. Argus, and S. Stein (1994), Effects of recent revisions to the geomagnetic reversal time scale on estimates of current plate motions, *Geophys. Res. Lett.*, *31*(20), 2191–2194.

Dengo, G. (1985), Mid America: Tectonic setting for the Pacific margin from southern Mexico to northwestern Clumbia, in *The Ocean Basins and Margins*, vol. 7A, edited by A. E. Nairn and F. G. Stechli, pp. 123–180, Plenum, New York.

Denyer, P., W. Montero, and G. E. Alvarado (2003), *Atlas Tectónico de Costa Rica*, Ed. de la Univ. de Costa Rica, San José.

DeShon, H. R., S. Y. Schwartz, S. L. Bilek, L. M. Dorman, V. Gonzalez, J. M. Protti, E. R. Flueh, and T. H. Dixon (2003), Seismogenic zone structure of the southern Middle America Trench, Costa Rica, *J. Geophys. Res.*, *108*(B10), 2491, doi:10.1029/2002JB002294.

Dinc, A. N. (2008), Local earthquake tomography of Central America: Structural variations and fluid transport in the

Nicaragua-Costa Rica subduction zone, Ph.D. thesis, Christian-Albrechts Univ. zu Kiel, Kiel, Germany.

Dinc, A. N., I. Koulakov, M. Thorwart, W. Rabbel, E. Flueh, I. Arroyo, W. Taylor, and G. Alvarado (2010), Local earthquake tomography of Central Costa Rica: Transition from seamount to ridge subduction, *Geophys. J. Int.*, in press.

Eaton, D. W., S. Dineva, and R. Mereu (2006), Crustal thickness and Vp/Vs variations in the Grenville orogen (Ontario, Canada) from analysis of teleseismic receiver functions, *Tectonophysics*, *420*, 223–238, doi:10.1016/j.tecto.2006.01.023.

Efron, B., and R. Tibshirani (1986), Bootstrap methods for standard errors, confidence intervals, and other measures of statistical accuracy, *Stat. Sci.*, *1*, 54–77.

Escalante, G. (1990), The geology of southern Central America and western Colombia, in *The Geology of North America*, vol. H, *The Caribbean Region*, edited by G. Dengo and J. E. Case, chap. 8, pp. 201–228, Geol. Soc. of Am., Boulder, Colo.

Feigenson, M. D., and M. J. Carr (1993), The source of Central American lavas: Inferences from geochemical inverse modeling, *Contrib. Mineral. Petrol.*, *113*, 226–235.

Frederiksen, A. W., and M. G. Bostock (2000), Modelling teleseismic waves in dipping anisotropic structures, *Geophys. J. Int.*, *141*, 401–412.

Gossler, J., R. Kind, S. V. Sobolev, H. Kämpf, K. Wylegalla, M. Stiller, and TOR Working Group (1999), Major crustal features between the Harz Mountains and the Baltic Shield derived fom receiver functions, *Tectonophysics*, *314*, 321–333.

Gräfe, K. (1998), Exhumation and thermal evolution of the Cordillera de Talamanca (Costa Rica): Constraints from fission track analysis, ^{40}Ar-^{39}Ar, and ^{87}Rb-^{87}Sr chronology, Ph.D. thesis, *Tübinger Geowiss. Arb. TGA A39*, Inst. für Geol. und Palaeontol., Tübingen, Germany.

Husen, S., R. Quintero, E. Kissling, and B. Hacker (2003), Subduction-zone structure and magmatic processes beneath Costa Rica constrained by local earthquake tomography and petrological modelling, *Geophys. J. Int.*, *155*, 11–32.

Jones, C. H., and R. A. Phinney (1998), Seismic structure of the lithosphere from teleseismic converted arrivals observed at small arrays in the southern Sierra Nevada and vicinity, *J. Geophys. Res.*, *103*, 10,065–10,090.

Kind, R., G. L. Kosarev, and N. V. Petersen (1995), Receiver functions at the stations of the German Regional Seismic Network (GRSN), *Geophys. J. Int.*, *62*, 191–202.

Kosarev, G., R. Kind, S. V. Sobolev, X. Yuan, W. Hanka, and S. Oreshin (1999), Seismic evidence for a detached Indian lithospheric mantle beneath Tibet, *Science*, *283*, 1306–1309.

Kussmaul, S. (2000), Estratigrafía de las rocas ígneas, in *Geología de Costa Rica*, pp. 63–86, Ed. Tecnol. de Costa Rica, San José.

LaFemina, P., T. H. Dixon, R. Govers, E. Norabueno, H. Turner, A. Saballos, G. Mattioli, M. Protti, and W. Strauch (2009), Fore-arc motion and Cocos Ridge collision in Central America, *Geochem. Geophys. Geosyst.*, *10*, Q05S14, doi:10.1029/2008GC002181.

Lewis, J. C., A. C. Boozer, A. López, and W. Montero (2008), Collision versus sliver transport in the hanging wall at the Middle America subduction zone: Constraints from background seismicity in central Costa Rica, *Geochem. Geophys. Geosyst.*, *9*, Q07S06, doi:10.1029/2007GC001711.

Linkimer, L., S. L. Beck, S. Y. Schwartz, G. Zandt, and V. Levin (2010), Nature of crustal terranes and the Moho in northern Costa Rica from receiver function analysis, *Geochem. Geophys. Geosyst.*, *11*, Q01S19, doi:10.1029/2009GC002795.

Lücke, O. H., H.-J. Götze, and G. E. Alvarado (2008), A constrained 3D density model of the upper crust from gravity data interpretation for central Costa Rica, *Int. J. Geophys.*, 860902, doi:10.1155/2010/860902.

MacKenzie, L., G. A. Abers, K. M. Fischer, E. M. Syracuse, J. M. Protti, V. Gonzalez, and W. Strauch (2008), Crustal structure along the southern Central American volcanic front, *Geochem. Geophys. Geosyst.*, *9*, Q08S09, doi:10.1029/2008GC001991.

Mann, P., R. D. Rogers, and L. Gahagan (2007), Overview of plate tectonic history and its unresolved tectonic problems, in *Central America: Geology, Resources and Hazards*, vol. 1, edited by G. Alvarado and J. Buntschuh, chap. 8, pp. 201–230, Taylor and Francis, London.

Marshall, J. S., D. M. Fisher, and T. W. Gardner (2000), Central Costa Rica deformed belt: Kinematics of diffuse faulting across the western Panama block, *Tectonics*, *19*(3), 468–492.

Meschede, M., and W. Frisch (1998), A plate-tectonic model for the Mesozoic and Early Cenozoic history of the Caribbean plate, *Tectonophysics*, *296*, 269–291.

Owens, T. J., G. Zandt, and S. R. Taylor (1984), Seismic evidence for an ancient rift beneath the Cumberland Plateau, Tennessee: A detailed analysis of broadband teleseismic P waveforms, *J. Geophys. Res.*, *89*(B9), 7783–7795.

Protti, M., F. Guendel, and K. McNally (1995), Correlation between the age of the subducting Cocos plate and the geometry of the Wadati-Benioff zone under Nicaragua and Costa Rica, in *Geologic and Tectonic Development of the Caribbean Plate Boundary in Southern Central America*, edited by P. Mann, *Spec. Pap. Geol. Soc. Am.*, *295*, 309–326.

Quintero, R., and E. Kissling (2001), An improved P-wave velocity reference model for Costa Rica, *Geofis. Int.*, *40*(1), 3–19.

Ramesh, D. S., H. Kawakatsu, S. Watada, and X. Yuan (2005), Receiver function images of the central Chugoku region in the Japanese islands using Hi-net data, *Earth Planets Space*, *57*, 271–280.

Ranero, C. R., and R. von Huene (2000), Subduction erosion along the Middle America convergent margin, *Nature*, *404*, 748–752, doi:10.1038/35008046.

Ryberg, T., and M. Weber (2000), Receiver function arrays: A reflection seismic approach, *Geophys. J. Int.*, *141*, 1–11.

Sallarès, V., J. J. Dañobeitia, E. R. Flueh, and G. Leandro (1999), Seismic velocity structure across the middle American landbridge in northern Costa Rica, *Geodynamics*, *27*, 327–344.

Sallarès, V., J. J. Dañobeitia, and E. R. Flueh (2001), Lithospheric structure of the Costa Rican Isthmus: Effects of subduction zone magmatism on an oceanic plateau, *J. Geophys. Res.*, *106*(B1), 621–643, doi:10.1029/2000JB900245.

Sallarès, V., P. Charvis, E. R. Flueh, and J. Bialas (2003), Seismic structure of Cocos and Malpelo Volcanic Ridges and implications for hot spot-ridge interaction, *J. Geophys. Res.*, *108*(B12), 2564, doi:10.1029/2003JB002431.

Savage, M. K. (1998), Lower crustal anisotropy or dipping boundaries? Effects on receiver functions and a case study in New Zealand, *J. Geophys. Res.*, *103*(B7), 15,069–15,087.

Schlindwein, V. (2001), Azimuthal variation of the P phase in Icelandic receiver functions *Geophys. J. Int.*, *144*, 221–230.

Sonderforschungsbereich 574 "Volatiles and Fluids in Subduction Zones" (SFB 574) (2003), SFB Progress Report (Phase 1), Christian-Albrechts-Univ. zu Kiel, Kiel, Germany.

Sodoudi, F. (2005), Lithospheric structure of the Aegean obtained from P and S receiver functions, Ph.D. thesis, Freie Univ. Berlin, Berlin.

Stavenhagen, A. U. (1998), Refraktionsseismische Untersuchungen on- und offshore Costa Rica, Ph.D. thesis, Christian-Albrechts-Univ. Kiel, Kiel, Germany.

Stavenhagen, A. U., E. R. Flueh, C. Ranero, K. D. McIntosh, T. Shipley, G. Leandro, A. Schulze, and J. J. Dañobeitia (1998), Seismic wide-angle investigations in Costa Rica—A crustal velocity model from the Pacific to the Caribbean coast, *Zentralblatt Geol. Palaontol, Teil 1*, *3–6*, 393–408.

Syracuse, E. M., G. A. Abers, K. Fischer, L. MacKenzie, C. Rychert, M. Protti, V. González, and W. Strauch (2008), Seismic tomography and earthquake locations in the Nicaraguan and Costa Rican upper mantle, *Geochem. Geophys. Geosyst.*, *9*, Q07S08, doi:10.1029/2008GC001963.

von Huene, R., C. R. Ranero, and W. Weinrebe (2000), Quaternary convergent margin tectonics of Costa Rica, segmentation of the Cocos Plate, and Central American volcanism, *Tectonics*, *19*(2), 314–334.

Walther, C. H. E. (2003), The crustal structure of the Cocos ridge off Costa Rica, *J. Geophys. Res.*, *108*(B3), 2136, doi:10.1029/2001JB000888.

Yamauchi, M., K. Hirahara, and T. Shibutani (2003), High resolution receiver function imaging of the seismic velocity discontinuities in the crust and uppermost mantle beneath southwest Japan, *Earth Planets Space*, *55*, 59–64.

Yuan, X., et al. (2000), Subduction and collision processes in the central Andes constrained by converted seismic phases, *Nature*, *408*, 958–961, doi:10.1038/35050073.

Zhu, L., and H. Kanamori (2000), Moho depth variation in southern California from teleseismic receiver functions, *J. Geophys. Res.*, *105*, 2969–2980.